Proton migration barriers in $BaFeO_{3-\delta}$ - Insights from DFT calculations

M. F. Hoedl, A. Chesnokov, D. Gryaznov, R. Merkle, E. A. Kotomin, J. Maier

Supplementary Information

1. Comparison of Volume and Shape Constraints

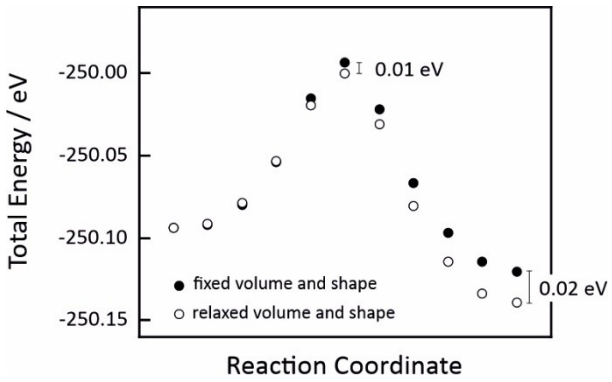

Figure S1: Comparison of energy profiles of NEB calculations in $Ba_8Fe_8O_{22}H$ with volume and shape fixed to starting geometry (filled symbols) and relaxed volume and shape of final geometry (open symbols). Full relaxation of final geometry leads to a lower total energy and barrier, but energy differences remain small.

2. Correlation of *p*-band center with Fe-O ICOHP

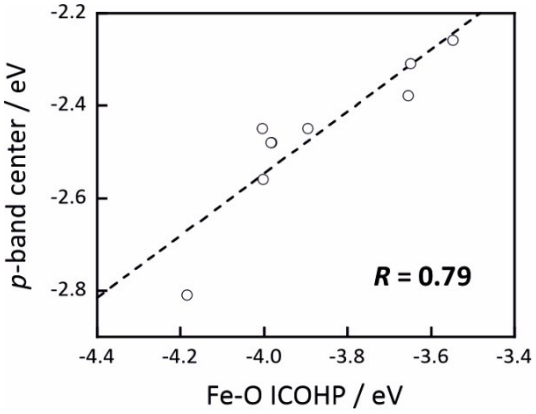

Figure S2: Correlation of *p*-band center of initial states with average Fe-O ICOHP (both Fe-O-Fe bonds, spin-up + spin-down). A higher bond covalency (more negative ICOHP) leads to a deeper *p*-band center.

3. Correlation of total energy with Mulliken Charge

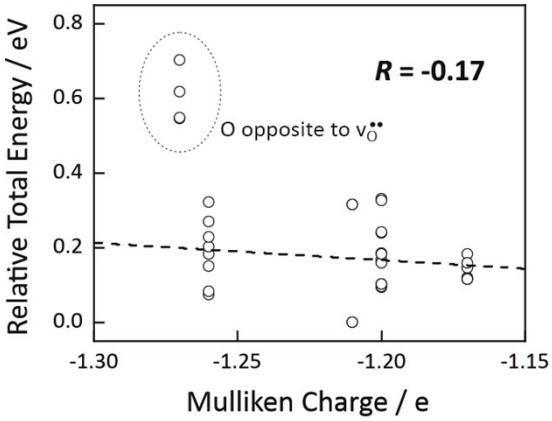

Figure S3: Correlation of relative total energies of a $Ba_8Fe_8O_{22}H$ supercell with the O-ion Mulliken charge in the dry state (prior to protonation).

4. Correlation of total energy with O-H bond length

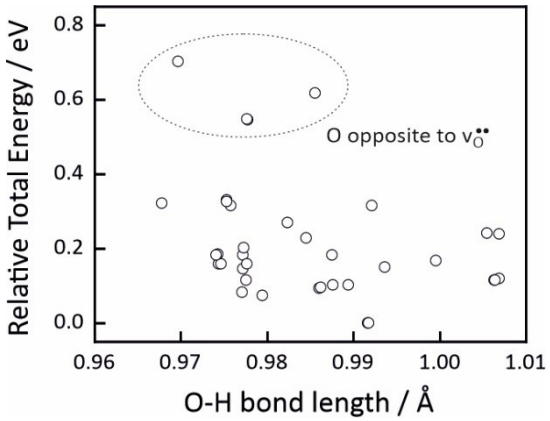

Figure S4: Correlation of relative total energies of a $Ba_8Fe_8O_{22}H$ supercell with the covalent O-H bond length.

5. Analysis of Bader atomic charges

Bader charges were calculated using the program developed by the Henkelman group[1] for the $Ba_8Fe_8O_{24}H$ and $Ba_8Fe_8O_{22}H$ supercells. The average calculated charges are listed in Tables S1 and S2 together with Mulliken charges obtained by our LOBSTER calculation for comparison. Overall, Bader charges yield reasonable charges and reflect the reduction of oxygen ions from -1.1 *e* in $Ba_8Fe_8O_{24}H$ to -1.2 e in $Ba_8Fe_8O_{22}H$. However, the individual Bader charges of Ba (not shown in Tables S1 and S2) exhibit a large scatter of 0.2-0.3 e, which is difficult to interpret since *A*-site cations in perovskite oxides are typically considered to be red-ox inactive and hardly involved in covalent interactions with the oxygen ions. Since Bader charges are sensitive to the number of grid points in the FFT grid, we tested different numbers of grid points, but could not find any convergence or trend in the obtained Bader charges. We therefore focused on the analysis of Mulliken charges rather than Bader charges. Additionally, in combination with DOS and COHP analysis, it is natural to use a wave function based charge partitioning method according to Mulliken rather than Bader charges.

Table S1: Comparison of Bader and Mulliken (LOBSTER) atomic charges for $Ba_8Fe_8O_{24}H$, averaged over the supercell.

$Ba_8Fe_8O_{24}H$	Bader / e	Mulliken / e
Ba	1.42	1.74
Fe	1.73	1.65
O	-1.05	-1.14

Table S2: Comparison of Bader and Mulliken (LOBSTER) atomic charges for $Ba_8Fe_8O_{22}H$, averaged over the supercell.

$Ba_8Fe_8O_{22}H$	Bader / e	Mulliken / e
Ba	1.52	1.72
Fe	1.64	1.64
O	-1.16	-1.24

6. Analysis of Fe and O magnetic moments

$BaFeO_3$ is characterized by a dominant $d^5\underline{L}$ ($\underline{L}$=ligand hole) configuration, which means that Fe majority spin-up *d*-states are largely occupied while the minority spin-down *d*-states are largely unoccupied.[2] This leads to relatively high local Fe magnetic moments (difference between Fe spin-up and spin-down states) of 4.0 μ_B on average. The states at the Fermi level, in turn, are primarily composed of oxygen 2*p* states such that a change in oxygen stoichiometry (and thus electron holes concentration) most strongly affects the charge of the oxygen ions. However, analysis of $Ba_8Fe_8O_{24}$, $Ba_8Fe_8O_{22}$ and $Ba_8Fe_8O_{20}$ supercells shows that, while the Fe Mulliken charges indeed remain relatively constant, there is a trend towards higher magnetic moments from ≈4.0 to ≈4.2 μ_B on average with increasing oxygen vacancy concentration. We therefore analyzed the projected DOS of Fe e_g-states in $Ba_8Fe_8O_{24}$, $Ba_8Fe_8O_{22}$ and $Ba_8Fe_8O_{20}$ supercells, see Figure S5, to explain the trend in local Fe magnetic moments.

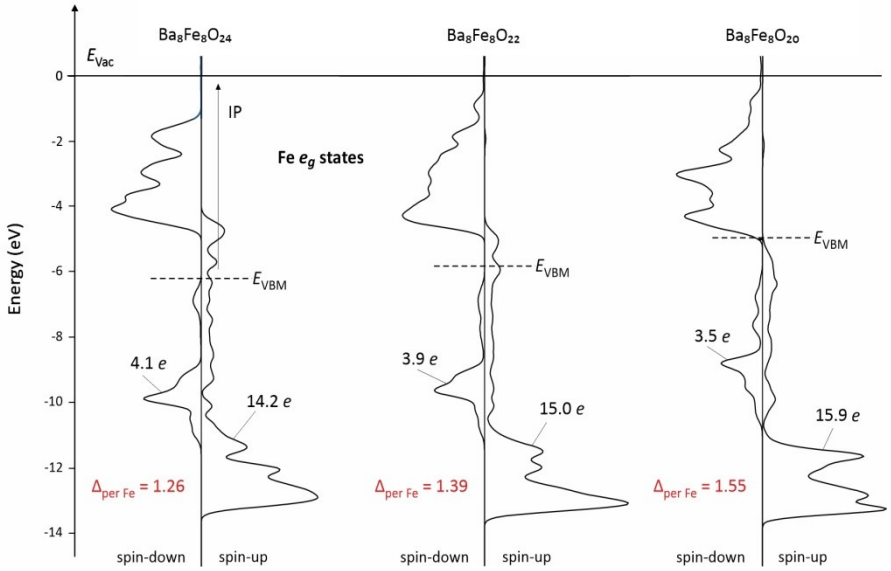

Figure S5: Projected density of states of $BaFeO_{3-\delta}$ with different oxygen stoichiometry, aligned to a common vacuum potential (see [3] for details of alignment procedure). Black curve shows Fe eg-states. Orbital populations are obtained by integration of the states up to the valence band maximum.

The e_g -states show one main peak for each spin component at ≈-12 eV in the spin-up and -≈-3 eV in the spin-down component. In addition, there are minor contributions in the realm of the O2p valence band between ≈-4 and ≈-10 eV, particularly a peak in the spin-down component at ≈-9 eV. These contributions result from a mixing of O2p and Fe3d states due to Fe-O covalent interactions. Upon increasing oxygen vacancy concentration, we observe two things: (1) the spin-up e_g -states at the Fermi level are filled up from 14.2 to 15.9 *e* due to an annihilation of electron holes and, (2) the fraction of occupied spin-down e_g states is reduced from 4.1 to 3.5 *e* due to less covalent Fe-O interactions as a consequence of the chemical expansion with increasing oxygen vacancy concentration. Thus, the magnetic moments increase within increasing oxygen vacancy concentration (higher occupation of spin-up states, lower occupation of spin-down states) while the Fe Mulliken charges remain relatively constant (cf. Tables S1 and S2). As such, magnetic moments and Mulliken charges are effectively decoupled in this system.

The connection between Fe-O covalency and Fe magnetic moments (by virtue of more or less occupied spin-down *d*-states) is also reflected in a correlation between Fe-O bond length (as proxy for the Fe-O bond covalency) and the Fe magnetic moment (see Figure S6). Here, two Fe species are distinguished depending on whether Fe is coordinated by an oxygen vacancy, i.e., in a square pyramidal [FeO_5] configuration, or whether Fe is part of a regular [FeO_6] octahedron. For a given Fe-

O bond length, the magnetic moment of Fe in an $[FeO_5]$ is higher than in a $[FeO_6]$ polyhedron. This could be attributed to a stronger reduction (electron hole annihilation) of atoms being closer to the oxygen vacancy and thus a higher occupation e_g spin-up states.

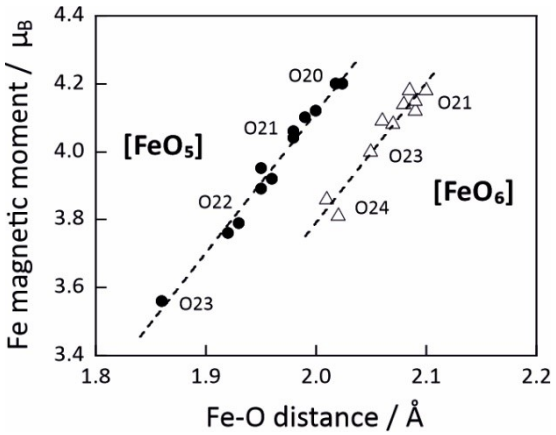

Figure S6: Correlation of Fe magnetic moment and Fe-O bond length. The labels O24, O23, O22, O21, O20 refer to oxygen stoichiometries in the respective supercells. The Fe-O bond distance is taken as an average of all nearest neighbor Fe-O bonds. If a supercell contains significantly different Fe local environments, they are indicated as separate data points

7. Downward Shift of *p*-band center upon protonation

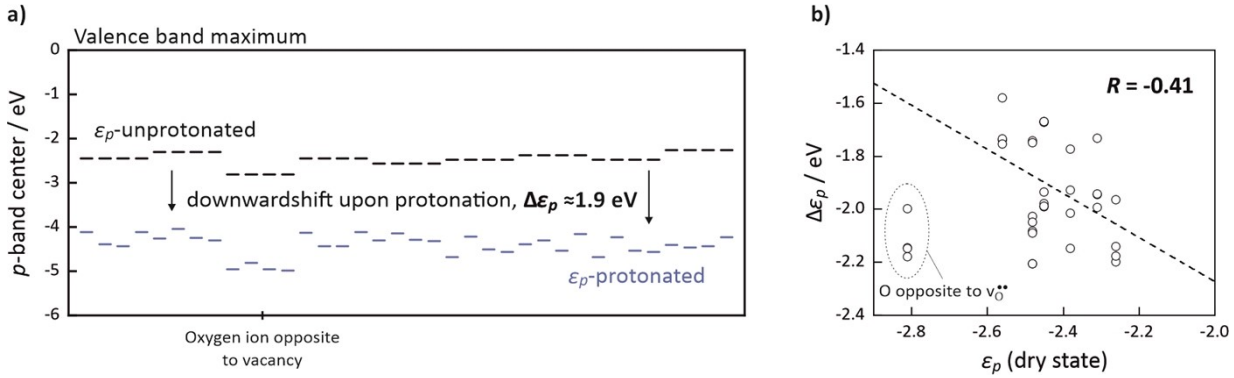

Figure S7: a) Downward shift of *p*-band center upon protonation. The data points represent different oxygen ions. Black: Unprotonated oxygen ions in a $Ba_8Fe_8O_{22}$ supercell; blue: protonated oxygen ions in $Ba_8Fe_8O_{22}H$ supercell. Each oxygen ion is probed with four different proton orientations that can lead to different ε_p in the protonated state. b) Downward shift of *p*-band center versus unprotonated p-band center.

8. Upward Shift of Fe-O ICOHP upon protonation

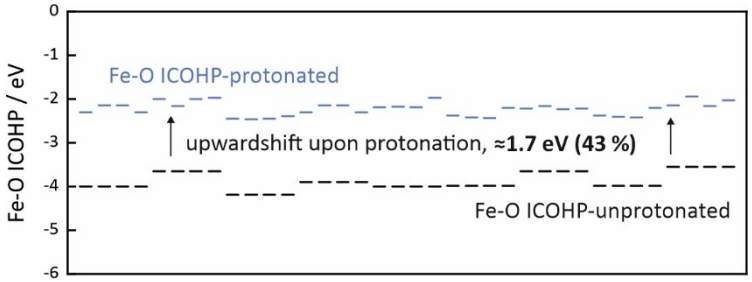

Figure S8: Upward shift of Fe-O ICOHP upon protonation. The data points represent two bonds of a Fe-O-Fe entity, for each bond spin-up and spin-down states are summed up. Black: Unprotonated $Ba_8Fe_8O_{22}$ supercell; blue: protonated $Ba_8Fe_8O_{22}H$ supercell. Each oxygen ion is probed with four different proton orientations that can lead to different a Fe-O ICOHP in the protonated state.

9. Relative Total Energies of Proton Transfer in O24 as a Function of O-O Distance

Typical initial state supercell dimensions are 8.38 Å ×8.03 Å ×7.96 Å for Fig. 5a,
8.37 Å ×7.95 Å ×8.05 Å for Fig. 5c.

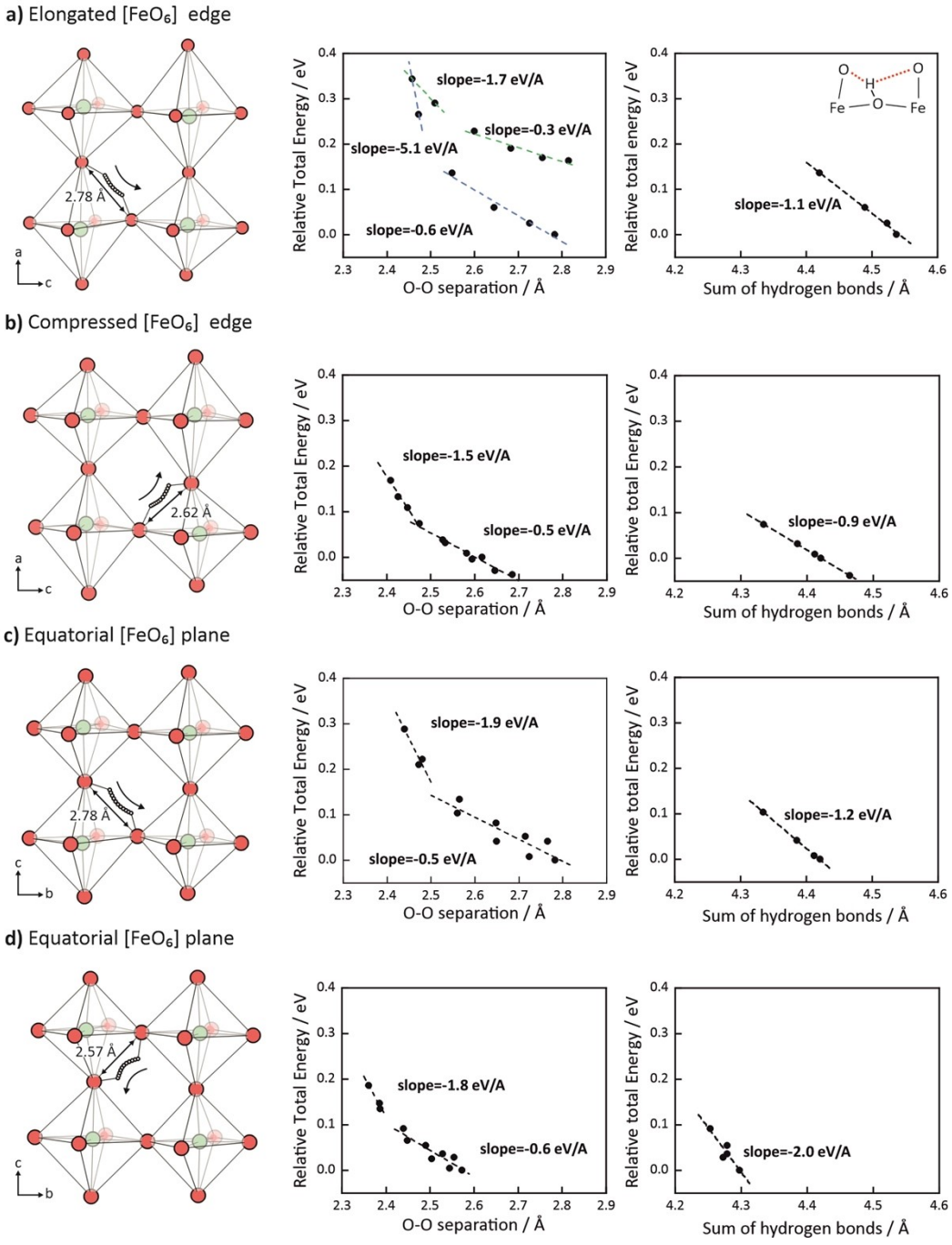

Figure S9: Different proton transfer trajectories $Ba_8Fe_8O_{24}H$ together with the relative total energy as a function of the O-O distance and as a function of the sum of hydrogen bond lengths. Since the trajectory for (a) is moderately asymmetric, the data points before and after the transition state are indicated by a different line pattern in the plot of relative total energy (relative to energy of initial state) vs. O-O separation. The right column shows the variation of total energy with the sum of the hydrogen bond lengths (using the first 3-4 images of each barrier). The slopes are mainly around 1 eV/Å; this is in good agreement with the scaling factor used in Fig. 3c to include the effect of hydrogen bond length on the total energy into the correlation plot of the protonation site preference.

10. Relative Total Energies of Proton Transfer in O22 as a Function of O-O Distance

Typical initial state supercell dimensions are 8.25 Å ×8.25 Å ×7.96 Å for Fig. 7b, 8.27 Å ×8.10 Å ×8.07 Å for Fig. 7d.

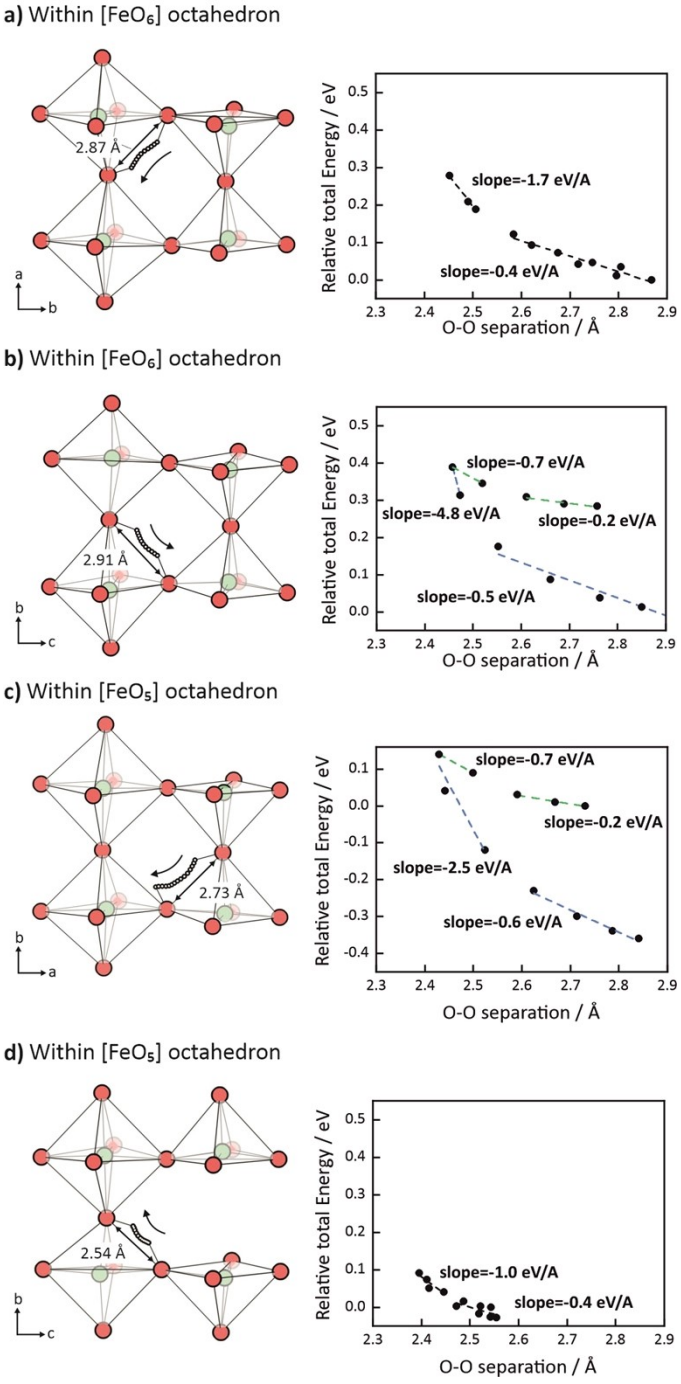

Figure S10: Different proton transfer trajectories $Ba_8Fe_8O_{22}H$ together with the relative total energy (relative to energy of initial state) as a function of the O-O distance. Since the trajectory for (c) and (d) are asymmetric, the data points before and after the transition state are indicated by a different line pattern.

11. Correlation of Proton Migration Barriers with initial O-O and O-H Distances

The two structural parameters that determine the height of the proton migration barrier – O-O and O-H distances – are not independent. Consider, for instance, the barriers labeled "1" and "2": while their O-O distances are virtually the same with 2.63 Å (1) and 2.64 Å (2), the barriers differ quite significantly with 0.18 eV (1) and 0.11 eV (2) (Figure S11a). The reason for the spread in migration barriers is due to different O-H bond lengths (Figure S11b), with a longer O-H bond in "2" leading to a lower barrier. Hence, deviations from the trend lines in Figures S11a,b can be explained by taking into account both structural parameters. The codependence of the proton migration barrier on both O-O and O-H distances is visualized in Figure S11c as a three-dimensional representation. At lower O-O distances, there is a greater variation in possible O-H bond lengths, particularly in the $Ba_8Fe_8O_{22}H$ supercell (yellow symbols), which – graphically speaking – pulls the surface in Figure S11c down toward the lower left corner.

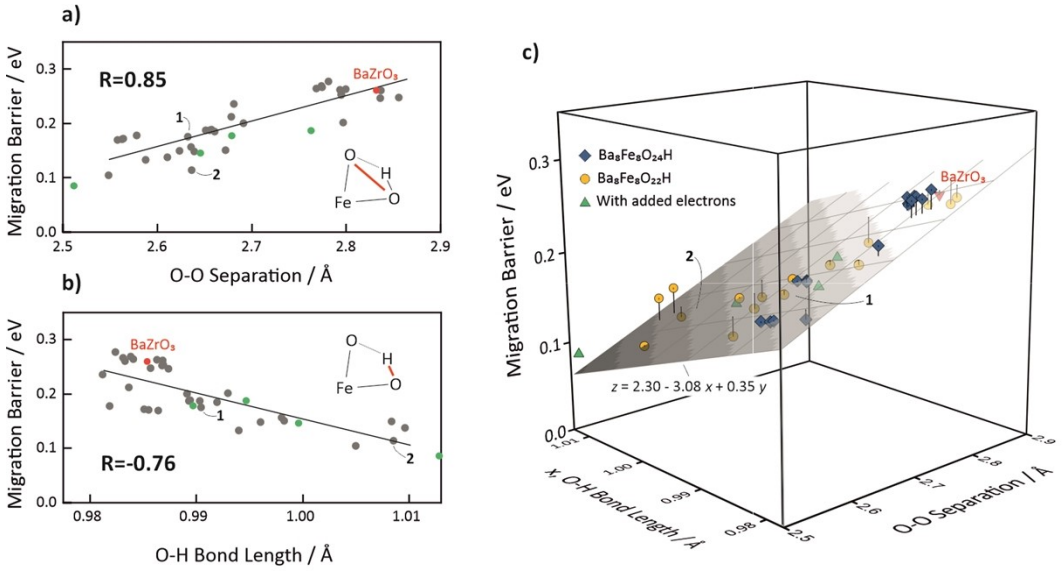

Figure S11: Correlation of proton migration barrier with the initial O-O distance (a), the initial O-H bond length (b), and both structural parameters in a three-dimensional graph (c). The term "initial" refers to an average of initial and final O-O and O-H distances. Green symbols represent data obtained from charged supercells, cf. Fig. 10b.

12. O-O and O-H Distances in Initial, Transition and Final States

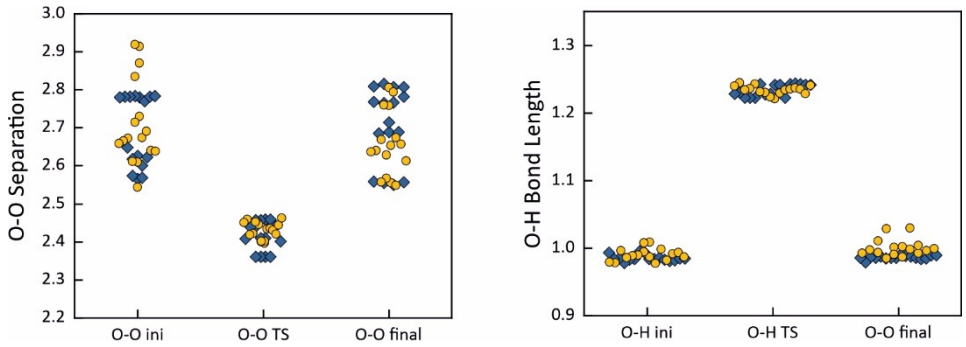

Figure S12: O-O distance and O-H bond length in initial, transition and final states (blue = $Ba_8Fe_8O_{24}H$ cells, yellow = $Ba_8Fe_8O_{22}H$ cells). The geometry in the transition state is characterized by very similar O-O and O-H distances for all supercells.

13. Symmetric and asymmetric energy profiles influenced by the isotropic strain

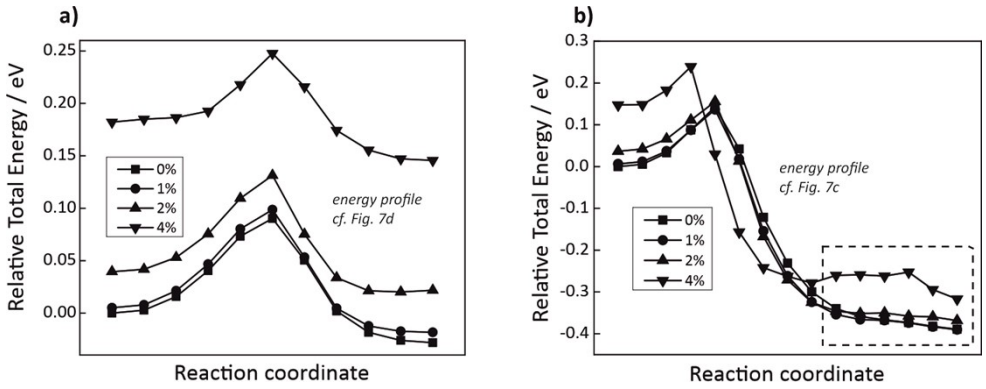

Figure S13: Migration profiles in the volume expansion (1%, 2%, and 4%) calculations for $Ba_8Fe_8O_{22}H$. The supercell total energy of the initial state of the unexpanded cell (0%) is taken as zero. (a) Symmetric profile corresponding to Fig. 7d. (b) Strongly asymmetric profile from Fig. 7c: here the NEB trajectory proceeds with a re-orientation; the dashed rectangle indicates the images where the re-orientation proceeds. The migration barriers discussed in Fig. 10a for asymmetric profile were obtained excluding the re-orientation part.

14. Symmetric and asymmetric energy profiles calculated for different oxidation states

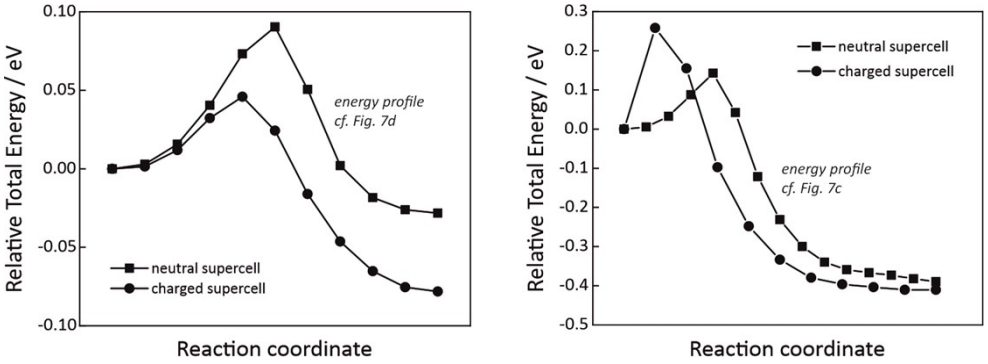

Figure S14: Migration profiles in charged supercell calculations for $Ba_8Fe_8O_{22}H$ (three electrons added, corresponding to all iron being formally Fe^{3+}). (a) Symmetric profile Fig. 7d. (b) Strongly asymmetric profile Fig. 7c. The supercell total energy of initial state is taken as zero for the neutral and charged supercells. Migration barriers as discussed in Fig. 11 for the asymmetric profile were obtained with exclusion of the re-orientation part (cf. Fig. S13b).

The transition state position is shifted closer to the initial point, i.e. to the part of the profile of higher energies, for the charged supercells in Fig. S14. In particular, the asymmetric profile in Fig. 7c is sensitive to this effect complicating the structural relaxation in the first few points of the profile.

15. Migration barrier as a function of formal oxidation state for highly asymmetric energy profile

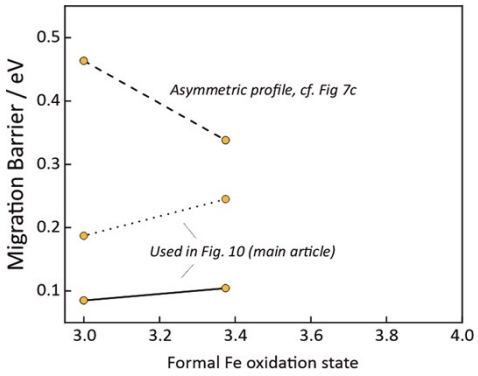

Figure S15: Proton migration barriers for highly asymmetric energy profile (cf. Fig. 7c main article) in $Ba_8Fe_8O_{22}H$ as a function of formal Fe oxidation state. Variation of oxidation state is achieved by adding electrons to supercells at fixed volume.

16. Proton Trajectory and Energy Profile in $BaZrO_3$

The dimensions of the initial state Ba8Zr8O24H supercell are 8.46 Å ×8.40 Å ×8.48 Å.

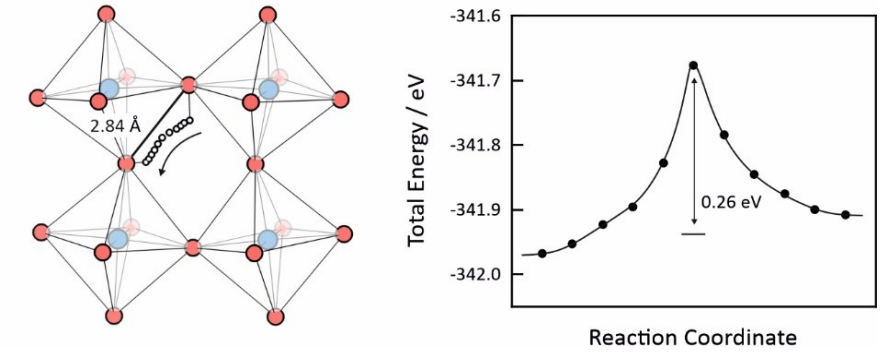

Figure S16: Proton transfer in $BaZrO_3$. Trajectory of proton transfer (left) and corresponding energy profile (right)

17. Comparison of DFT+U and HSE calculations

In order to validate the present DFT+U approach (U_{eff} = 4 eV for Fe), we carried out several calculations using the HSE06 hybrid DFT functional[4,5]. In particular, we calculated 3 protonated supercells, where the proton is located at different oxygen ions and plotted the total energies of these supercells as a function of the unprotonated oxygen p-band center, in analogy to Figure 3 of the main paper, see Figure S17 (total energies are given relative to the lowest total energy of the three calculated supercells). The data in Figure S17 demonstrates that the trend of proton site preference as a function of the unprotonated oxygen p-band center in $BaFeO_{3-\delta}$ is consistent between PBE+U (slope = -0.76) and HSE06 (slope = -0.84). However, absolute values of p-band centers may differ depending on the choice of the functional.

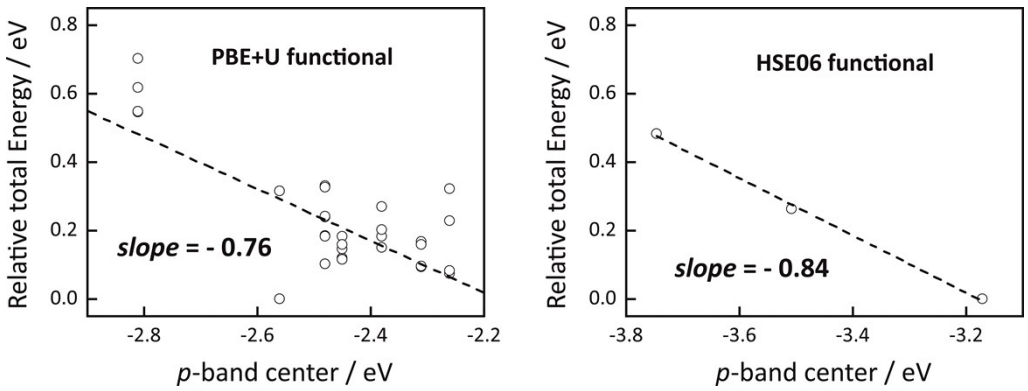

Figure S17: Total energies of $Ba_8Fe_8O_{22}H$ supercells with H attached to different oxygen ions as a function of the oxygen *p*-band center prior to protonation (i.e. in the respective $Ba_8Fe_8O_{22}$ supercell). Left: PBE+*U* (U_{eff} = 4 eV per Fe), right: HSE06 functional.

Several proton migration barriers were selected for the comparison of the DFT+*U* functional (used throughout the present paper) with the hybrid HSE06 functional such that they cover small and large as well as more or less symmetrical barriers. The barrier in $BaZrO_3$ is also included. The NEB energy profiles are shown in Figure S18, relevant numbers are compiled in Table S3.

Table S3: Comparison of selected hybrid HSE06 functional results to PBE+U data (cf. Fig, 5a,c and Fig. 7b,d). The first lines give the change in supercell volume *V* and respective change of pseudocubic lattice parameter *a*. The next lines give the average of initial/final state O-H distance *d*(O-H), the transition state O-H distance (average of the two O-H lengths in the transition state), and the respective differences between HSE06 and PBE. The distance *d*(O···O) of the two oxygens closest to the proton and the kinetically averaged (KRA) proton migration barriers are also given.

	O24 Fig. 5a	O24 Fig. 5c	O22 Fig. 7b	O22 Fig. 7d	$BaZrO_3$ Fig. S16
$(V_{HSE}-V_{PBE})/V_{PBE}$ / %	-4.0	-3.7	-3.4	-3.3	-2.5
$(a_{HSE}-a_{PBE})/a_{PBE}$ / %	-1.3	-1.2	-1.2	-1.1	-0.8
initial/final *d*(O-H) PBE / Å	0.987	0.984	0.987	1.009	0.983
initial/final *d*(O-H) HSE / Å	0.970	0.968	0.968	0.992	0.971
difference / %	-1.7	-1.6	-1.9	-1.6	-1.2
transition state *d*(O-H) PBE / Å	1.242	1.240	1.240	1.220	1.240
transition state *d*(O-H) HSE / Å	1.229	1.231	1.229	1.204	1.225
difference / %	-1.1	-0.7	-0.9	-1.3	-1.2
initial/final *d*(O···O) PBE / Å	2.79	2.77	2.84	2.54	2.86
initial/final *d*(O···O) HSE / Å	2.81	2.78	2.92	2.53	2.80
difference / %	+0.7	+0.4	+2.8	-0.4	-2.1
transition state *d*(O···O) PBE / Å	2.46	2.44	2.46	2.41	2.44
transition state *d*(O···O) HSE / Å	2.44	2.42	2.44	2.38	2.41
difference / %	-0.8	-0.8	-0.8	-0.8	-1.3
migration barrier PBE / eV	0.26	0.27	0.25	0.10	0.26
migration barrier HSE / eV	0.37	0.37	0.35	0.13	0.31
difference /eV	0.11	0.10	0.10	0.03	0.05

With HSE06, the volumes of BF O24 and O22 supercells are decreased by 3.3-4%, which corresponds to a decrease of the pseudocubic lattice parameter of 1.1-1.3%. It is important to note that the averaged initial/final O-H distances decrease significantly stronger, by 1.6-1.9 % (0.16-0.19 Å). It has been observed also in other investigations that hybrid functionals yields shorter O-H covalent bonds than GGA functionals, and that the energy required for stretching this bond is higher when calculated with hybrid functionals.[6]

In contrast to the initial/final O-H bond length, the O-H distance in the transition state decreases less than the pseudocubic lattice parameter. Also the averaged initial/final O···O distance shrinks less or even increases. This means that, relatively speaking, the initial/final O-H bond length is contracted (i.e. strengthened) more than the transition state O-H distance, which results in an increased migration barrier. The fact that the initial/final O···O distance shrinks less than the pseudocubic lattice parameter or even increases also contributes to the barrier increase. For the different $BaFeO_{3-\delta}$ cells, this results in a proton migration barrier increase of ≈0.1 eV when using HSE06 compared to PBE+*U*, but the trends observed in Figs. 9 and S11 (increase of barrier with increasing O···O and decreasing O-H distance) remain intact. Thus, the change of functional does not affect the main conclusions drawn from the PBE+*U* calculations.

A slightly smaller change of cell volume and initial/final O-H distance is observed for $BaZrO_3$, i.e. the difference between the functionals originates not only from a different treatment of iron d electrons but comprise the whole electronic structure. However, for $BaZrO_3$ the transition state O-H bond shows a comparable contraction as the initial/final O-H bonds, and the initial/final O···O is even slightly shortened, thus the increase of migration barrier when using HSE06 is less pronounced (+0.05 eV).

In conclusion, both functionals – PBE+*U* and HSE06 – yield very similar results regarding proton site preference and variations in proton migration barriers. This proves the general validity of the DFT+*U* approach for proton-related properties.

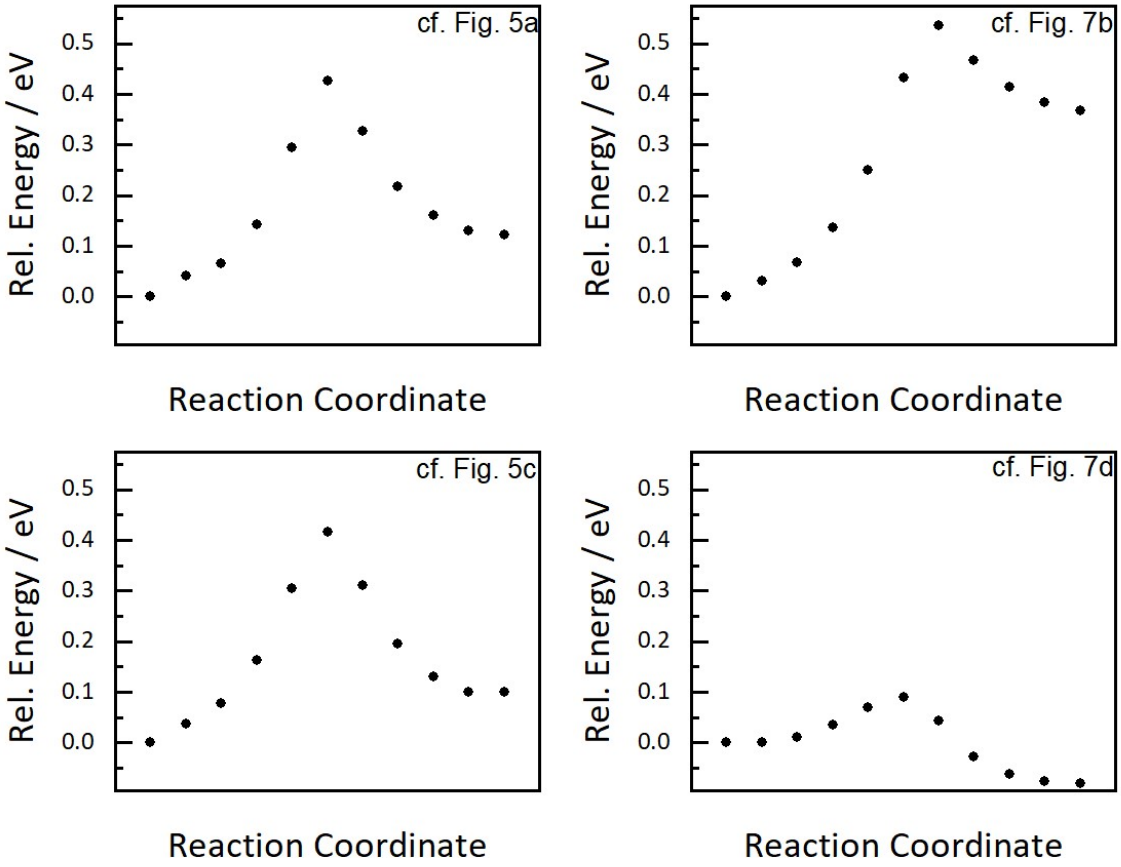

Figure S18: Selected proton migration energy profiles in $BaFeO_{3-\delta}$ calculated with the hybrid HSE06 functional (see Fig, 5a,c and Fig. 7b,d for the respective PBE+U barriers).

References

[1] W. Tang, E. Sanville, and G. Henkelman, A grid-based Bader analysis algorithm without lattice bias, *J. Phys.: Condens. Matter*, 2009, **21**, 084204.

[2] M. F. Hoedl, C. Ertural, R. Merkle, R. Dronskowski and J. Maier, The Orbital Nature of Electron Holes in $BaFeO_3$ and Implications for Defect Chemistry, *J. Phys. Chem. C*, 2022, **126**, 12809-12819.

[3] M. F. Hoedl, D. Gryaznov, R. Merkle, E. A. Kotomin, and J. Maier, Interdependence of Oxygenation and Hydration in Mixed-Conducting $(Ba,Sr)FeO_{3-\delta}$ Perovskites Studied by Density Functional Theory, *J. Phys. Chem. C*, 2020, **124**, 11780−11789.

[4] J. Heyd, G.E. Scuseria and M. Ernzerhof, Hybrid functionals based on a screened Coulomb potential. *J. Chem. Phys.*,2003, **118**, 8207-8215.

[5] J. Heyd, G.E. Scuseria and M. Ernzerhof, Erratum:"Hybrid functionals based on a screened Coulomb potential"[J. Chem. Phys. 118, 8207 (2003)]. *J. Chem. Phys.*, 2006, **124**, 219906.

[6] M.J. Gillan, D. Alfe, A. Michaelidis, Perspective: How good is DFT for water? *J. Chem. Phys*., **2016**, 144, 130901.